Available online at www.sciencedirect.com
SCIENCE DIRECT®
Journal of Computational and Applied Mathematics 197 (2006) 122–140
JOURNAL OF COMPUTATIONAL AND APPLIED MATHEMATICS
www.elsevier.com/locate/cam

A hybrid technique for computing the power distribution generated in a lossy medium during microwave heating

V. Vegh[a,*], I.W. Turner[b]

[a] *Centre for Magnetic Resonance, University of Queensland, Research Road, St Lucia QLD 4072, Australia*
[b] *School of Mathematical Sciences, Queensland University of Technology, George Street, Brisbane QLD 4001, Australia*

Received 12 February 2003; received in revised form 7 July 2005

Abstract

Over the years researchers in the field of computational electromagnetics (CEM) have investigated and explored a number of different techniques to resolve electromagnetic fields inside waveguide and cavity structures. The equations that govern the fundamental behaviour of electromagnetic wave propagation in such structures are Maxwell's equations. In the literature, a number of different techniques have been employed to solve these equations and out of these methods, the classical finite-difference time-domain (FD-TD) scheme, which uses a staggered time and space discretisation, is the most well-known and widely used. However, this scheme is complicated to implement on an irregular computational domain using unstructured meshes.

This research work builds upon previous work undertaken for a waveguide, where a coupled method was introduced for the solution of the governing electromagnetic equations. In that work, the free-space component of the solution was computed in the time-domain, whilst the power distribution in the load was resolved using the frequency dependent electric field Helmholtz equation. This methodology resulted in a time-frequency domain hybrid scheme. In this paper, the hybrid method has been tested further for both waveguide and cavity configurations that are loaded with a lossy dielectric material. Numerical tests highlight both the accuracy and computational efficiency of the proposed hybrid strategy for predicting the power distribution generated during microwave heating processes. The accuracy of the hybrid scheme is gauged by direct comparison with the FD-TD numerical solutions and previously published thermal images.

Keywords: CEM; DFT; Hybrid; Helmholtz; Maxwell

1. Introduction

The development of technological advances in the Sciences and Computing [6,8] has seen the requirement to resolve ever-greater applications in electromagnetics. Applications of electromagnetic energy range from satellite communication systems and stealth detection in the defences to communication of data between geographically displaced locations in Information Technology, and to tree root sterilisation in the sewage industry. Most of the applications, in one form or another, can be decomposed into a subset of local problems in electromagnetic theory [11,7]. For example, in microwave wood drying, the electromagnetic field behaviour outside of the domain of wood (referred to as the exterior

* Corresponding author. Tel.: +61 7 3365 7076; fax: +61 7 3365 3833.
E-mail address: v.vegh@uq.edu.au (V. Vegh).

0377-0427/$ - see front matter © 2005 Elsevier B.V. All rights reserved.
doi:10.1016/j.cam.2005.10.031

problem) is of little interest, and the problem should be focused primarily on predicting the heating or power distribution generated inside the material [23] (the interior problem). In such circumstances, it is only natural to develop methods that can concentrate the computational impetus on the interior problem and obtain solutions to these accurately and efficiently. The hybrid method [19,18] is one such method that enables the electromagnetic fields evolving within the interior problem to be solved at a relatively high resolution, and reduces the often exhaustive computational overheads associated with the exterior domain.

The new hybrid approach proposed in [19] for resolving the electromagnetic phenomena in a waveguide structure is based on the coupling of a time-marching Maxwell's equation numerical solver and a frequency-domain Helmholtz equation solution. In the past, both the time-domain and frequency-domain techniques have been applied individually, without coupling, to study a variety of microwave heating applications [23,17,10,3,16]. When solely using time-domain numerical solvers like the finite-difference time-domain (FD-TD) method [21], some restrictions on the problem have to be imposed (for example mesh size and element shape), so that a convergent solution can be obtained. In some problems the irregular shape of both the apparatus and load restrict the numerical solver from obtaining accurate solutions to the electromagnetic field evolutions, and consequently, other methods are sought to better capture the nature of the electric and magnetic field components.

Typically, in the FD-TD method the errors for the discretisations are minimised because of the staggering of the spatial locations of the electric and magnetic field components to cell edges and cell faces, respectively, and the positioning of the electric and magnetic fields are at different time levels. Over the last decade there have been a number of modifications made to the FD-TD method to better its performance through revision of reflected and refracted waves at material interfaces [22], and by applying different types of absorbing boundary conditions [1,12]. Unfortunately, FD-TD cannot be implemented on unstructured grids in a straightforward manner [22]. Researchers are attempting to generalise the FD-TD solution strategy for use on an unstructured domain [23], but such work has not been entirely successful. The main complexity arises due to the construction of the dual cell, which for general unstructured meshes sees the normal vectors to the primary cell faces not aligned with the edges of the dual cell [24,4,9].

Frequency or time-harmonic numerical methods possess different restrictions when the frequency dependent electromagnetic theory is applied to industrial microwave heating problems. The classical Helmholtz equation [7], which is derived from the time-harmonic magnetic and electric field point relations, can be used to obtain the electric fields inside the material and free-space, without having to compute the magnetic fields. On the other hand, in the time-domain solvers, both electric and magnetic fields must be computed. The advantage of the Helmholtz equation is that the power distribution is obtained easily from the frequency domain solution of the electric field, without the need to compute the magnetic field. It is well-known that time-marching schemes require a fairly large number of electromagnetic wave period computations before adequate power distributions can be obtained [23]. It is also well-known that time-harmonic schemes tend to generate coefficient matrices in the implicit solution strategy that are highly ill-conditioned, and hence, require innovative and computationally intensive numerical techniques to obtain a solution to the problem [3]. Consequently, both time and frequency domain strategies have restrictions that constrain the numerical performance of the underlying electromagnetic algorithm.

Unlike the FD-TD method, which marches the solution in time according to some stability criterion imposed due to both material and grid properties, the Helmholtz equation solution strategy presents a system of linear equations. This system of linear equations is sparse and, as mentioned above, often ill-conditioned, with the severity of the ill-conditioning depending on the boundary condition used and the type and location of the material inside the cavity [3]. There are numerous techniques available to solve systems of linear equations, some of these include factorising the coefficient matrix into lower and upper triangular matrices (LU), bi-conjugate gradient stabilised (biCGstab), quasi-minimal residual (QMR) and generalised minimal residual (GMRES). Depending on the solver used, preconditioning to reduce the condition number of the coefficient matrix may be required [14].

In the solution strategy of the Helmholtz equation, adaptive preconditioners are sometimes needed to cater for the changing frequencies and the different material interfaces. To obtain electric fields and thereafter power distributions, it is not enough to use a single (so-called dominant) frequency to obtain the solution in the frequency-domain, but rather, it may be necessary to compute energy levels that consist of a number of neighbouring frequencies around the dominant mode that approximate the three electric field components in the frequency domain.

The hybrid method [19,18] aims to eliminate some of the restrictions of the FD-TD method and the Helmholtz equation solver. To do this, the hybrid method takes advantage of the sparsity of the nodes in free-space and uses problem decomposition to reduce the condition number of the matrix in the domain of the load. A cell-centred in

finite-volume time-domain (ccFV-TD) solver that works well in free-space [20] is used to obtain the electric and magnetic field outside the load (see Fig. 2) on a relatively coarse mesh. The time-domain electric field distribution solution is converted to the frequency-domain electric fields at the load boundary via the discrete Fourier transform (DFT). This information is obtained not only at a single frequency, but rather for a set of frequencies in the neighbourhood of the dominant frequency. Once the interface boundary information is computed, the Helmholtz equation is solved a number of times with the generated boundary conditions at the various discrete frequencies.

The resulting system of linear equations is no longer as ill-conditioned as a system that resolves the whole domain (i.e., free-space and load), because only the load has been discretised and a system of linear equations is generated with Dirichlet interface boundary conditions between the free-space and the material with acceptable accuracy. Subsequently, a smaller system of linear equations is formulated that converges to a stable solution more rapidly than a system that is representative of the domain of free space and the load together. As a result, the hybrid method for multi-mode cavity structures yields a technique that provides efficient generation of load boundary information, since the time-domain solver used is applied on a coarse grid, and hence, the solution of the electric field is computed rapidly.

This paper firstly consists of an outline of the hybrid method, followed by an outline of the boundary condition treatment, after which a number of case studies are presented in the results section. Finally, the main conclusions of the research work are summarised. The research work shows that the hybrid method is accurate and highly efficient for predicting the power distribution inside lossy materials during microwave heating processes. The findings are validated for two waveguide case studies and two different industrial case studies using thermal images.

2. Outline of the hybrid method

The aim of the numerical scheme is to resolve the power distribution inside the load, so that the power can be coupled (if so desired) with the forced heat equation to obtain the temperature distribution. The scope of this paper is to demonstrate that the previously published hybrid method can be used successfully for a waveguide and multi-mode cavity to predict the power distribution in a lossy load located inside the full field region of the guide and the cavity.

Fig. 1 illustrates the waveguide and location of the load. In the figure, a, b and c are the dimensions of the rectangular waveguide. The cavity problem (see Fig. 12) is an extension of the waveguide problem, where another larger rectangular section has been attached to the end of the waveguide. P is the size of the perfectly matched layer (PML) boundary region that absorbs any impinging waves in the scattered (S) field region of the guide that may be reflected from the full (F) field region. The waveguide is decomposed into two domains, namely D_1, which is the free-space component, and D_2 representing the load. In Fig. 1, the input plane propagates a TE_{10} electromagnetic wave at 2.45 GHz into the full field region of the guide.

The hybrid method is a numerical technique that comprises the solution of two decoupled problems, which are referred to as the exterior and the interior problems. The exterior problem requires the solution of the time-dependent Maxwell's equations to be solved to approximate the fields inside the free-space (D_1) and on the material interface. Whereas, the

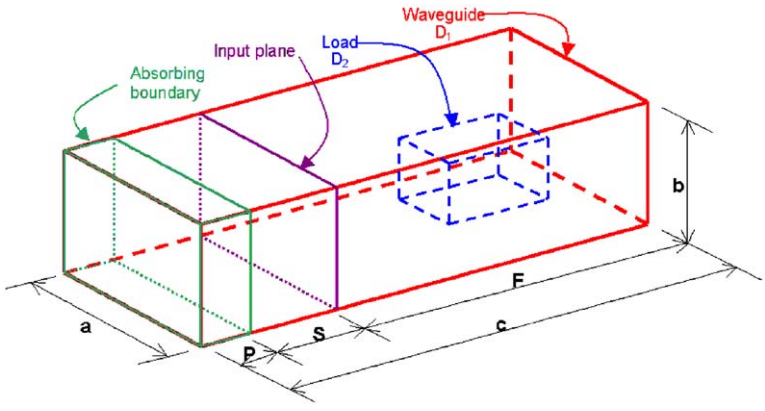

Fig. 1. The loaded waveguide and dimensions.

interior problem requires the solution to the electric Helmholtz equation and thereafter the power distribution inside the load (D_2). The following two sections outline the exterior and interior problem methodologies in detail.

2.1. Exterior problem—Maxwell's equations

In the free space component (D_1), the electric and magnetic fields are governed by Maxwell's equations [7]. The time-dependent equations are represented as

$$\nabla \times \mathbf{E} = -\frac{\partial \mathbf{B}}{\partial t}, \quad \nabla \times \mathbf{H} = \frac{\partial \mathbf{D}}{\partial t} + \mathbf{J}, \tag{1}$$

$$\mathbf{B} = \mu \mathbf{H}, \quad \mathbf{D} = \varepsilon \mathbf{E}, \quad \mathbf{J} = \sigma \mathbf{E}, \quad \varepsilon = \varepsilon_0 \varepsilon', \quad \sigma = \omega \varepsilon_0 \varepsilon''. \tag{2}$$

In this paper, (1) is solved using a cell-centred finite-volume time-domain numerical solver. This time-marching scheme uses a Leapfrog time stepping technique and for the finer details of the implementation the reader is referred to [20]. The second order in space cell-centred Leapfrog time-marching algorithm at a point is given as

$$\mathbf{H}_p^{n+1/2} = \mathbf{H}_p^{n-1/2} - \frac{\Delta t}{\mu_0 \Delta V} \sum_{f \in \zeta_p} (\mathbf{n} \times \mathbf{E})_f^n \Delta S_f, \tag{3}$$

$$\mathbf{E}_p^{n+1} = \frac{2\varepsilon - \sigma \Delta t}{2\varepsilon + \sigma \Delta t} \mathbf{E}_p^n + \frac{2\Delta t}{(2\varepsilon + \sigma \Delta t)\Delta V} \sum_{f \in \zeta_p} (\mathbf{n} \times \mathbf{H})_f^{n+1/2} \Delta S_f. \tag{4}$$

In (3) and (4) p represents the pth cell inside the computational domain, f is a cell face unknown (on a structured grid determined simply by taking the average value of adjacent cells) of cell p and ζ_p is the set of faces that constitute the pth cell. Δt, ΔS_f and ΔV are the time step of the numerical scheme, surface area of face f and volume of cell p, respectively. Eqs. (3) and (4) are applied to solve for the electric and magnetic field components inside the free-space part of the waveguide, in which case the time marching steps are governed by the Courant–Friedrichs–Lewy condition that for structured grids is given as

$$\Delta t \leqslant \sqrt{\frac{\mu_0 \varepsilon_0}{1/\Delta x^2 + 1/\Delta y^2 + 1/\Delta z^2}}, \tag{5}$$

where Δx, Δy and Δz are the Cartesian discretisation cell dimensions.

2.2. The material interface

Eqs. (3) and (4) purely simulate the free-space electromagnetic behaviour, and are used only to generate the boundary condition information for the interior problem, which is then transformed to the frequency domain via the discrete Fourier transform [13] at the material interfaces:

$$\phi^k = \int_{-\infty}^{+\infty} \mathbf{F}(t) \mathrm{e}^{2\pi \mathrm{i} f_k t} \, \mathrm{d}t \approx \sum_{n=0}^{N-1} \mathbf{F}^n \mathrm{e}^{2\pi \mathrm{i} f_k t_n / N} \Delta t = \Delta t \sum_{n=0}^{N-1} \mathbf{F}^n \mathrm{e}^{2\pi \mathrm{i} k n / N}, \tag{6}$$

where

$$f_k = \frac{k}{N \Delta t}, \quad \phi^k = \phi(f_k), \quad t_n = n \Delta t, \quad k = -\frac{N}{2} \cdots \frac{N}{2}. \tag{7}$$

In (6) and (7), $\mathbf{F}^n$ is the discrete set of electric and magnetic field components as computed by (3) and (4). The DFT algorithm is used to transform time-domain electric field values that lie on the interface between the material and free-space. In the frequency domain, $\phi(f_k)$ is the electric and magnetic field at the f_k frequency. The load and boundary data generation are illustrated in Fig. 2.

It should be noted that the exterior problem is assumed to have converged once the exterior fields exhibit a stable periodic behaviour. At this point, the time domain fields are converted to the frequency domain on all material interfaces.

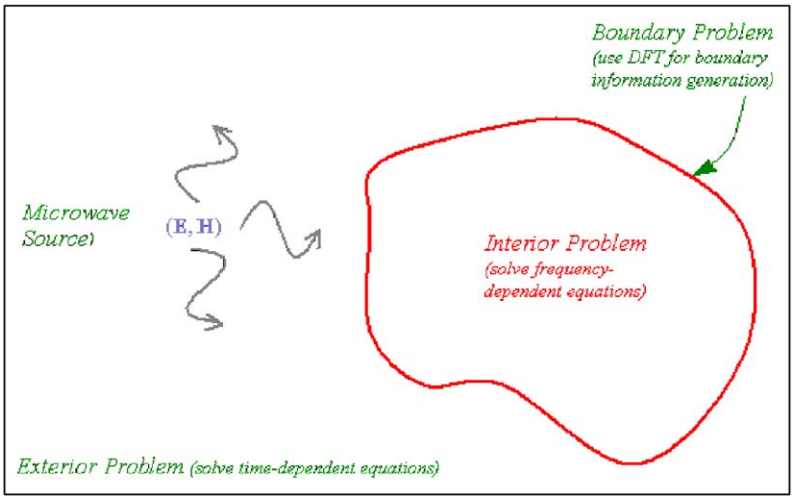

Fig. 2. Solution methodology for the interior problem.

If the transient behaviour is not achieved in the exterior region to the material, then it is not possible to obtain sufficiently accurate information for the interior problem. Therefore, a method to determine transient behaviour must be adopted. A number of different options can be implemented to determine whether or not the electromagnetic waves depict transient behaviour; however, in this work a strategy was used that simply monitors the changes from wave period to wave period, and if no sufficient change in the oscillations is observed, then the information from the following simulated period is converted to the frequency domain.

2.3. Boundary conditions

In the previous subsection the exterior problem of the hybrid method was discussed in detail. In this subsection the boundary conditions for the free-space conducting wall, input-plane, perfectly matched layer and material interface are formulated, which are relevant for the exterior problem.

In the free space region (D_1) of the waveguide, a 2.45 GHz TE_{10} electromagnetic wave is generated according to

$$E_y^I = \text{Gauss}(t) E_0 \sin\left(\frac{\pi x}{a}\right) \cos(\omega t - \beta_0 z_0), \tag{8}$$

$$H_x^I = -\text{Gauss}(t) \frac{\beta_0}{\omega \mu_0} E_0 \sin\left(\frac{\pi x}{a}\right) \cos(\omega t - \beta_0 z_0), \tag{9}$$

$$H_z^I = -\text{Gauss}(t) \frac{\pi}{\omega \mu_0 a} E_0 \cos\left(\frac{\pi x}{a}\right) \sin(\omega t - \beta_0 z_0), \tag{10}$$

$$\beta_0 = \sqrt{\omega^2 \mu_0 \varepsilon_0 - \left(\frac{\pi}{a}\right)^2}, \quad \text{Gauss}(t) = \begin{cases} e^{-(t-3T)^2/T^2}, & t \leqslant 3T, \\ 1, & t > 3T. \end{cases} \tag{11}$$

The Gaussian function in (8)–(10) is used to smoothen the incident waves so that the noise due to the input plane is minimised [23]. At the input plane the fields are implemented according to [20]. Initially the unknowns for the magnetic and electric field components are set to zero and the electromagnetic field is propagated using the input boundary condition.

Generally for this situation, the incident fields propagate into the full field region of the guide (and into the cavity), after which they are reflected back from the material and cavity walls into the scattered field region. Any reflected waves that impinge into the scattered region must be absorbed and here, a perfectly matched layer absorbing boundary condition is implemented [12] to achieve this. The implementation details of the Petropolous PML with the SLF Maxwell's equation discretisation in the framework of a finite-volume methodology for a waveguide is derived in [20].

It should be noted that since this study investigates the hybrid method for a generalised cavity problem, the Petropolous PML is somewhat different to [20]. In this case, not only the previously implemented PML is used, but also another PML region is created to ensure that at the input plane only the true TE_{10} fields exist (i.e., H_x, H_z, and E_y). The formula for the PML region is given by the following equation [20]:

$$\mathbf{H}_p^{n+1/2} = \mathbf{H}_p^{n-1/2} - \left(\frac{2\mu_0\Delta t + \sigma^*\Delta t^2}{2\mu_0^2\Delta V}\right)\sum_{f\in\zeta_p}(\mathbf{n}\times\mathbf{E})_f^n\Delta S_f - \frac{\sigma^*\Delta t^2}{\mu_0^2\Delta V}\mathbf{F}_p^{n-1}, \tag{12}$$

$$\mathbf{F}_p^n = \mathbf{F}_p^{n-1} + \sum_{f\in\zeta_p}(\mathbf{n}\times\mathbf{E})_f^n\Delta S_f. \tag{13}$$

In (12), $\sigma^* = (\mu_0/\varepsilon_0)\sigma$ is chosen to ensure that as the waves impinge further into the perfectly matched layer the absorptivity (σ) of the material increases [12]. Similarly, the normal component of the electric field within the PML region is defined as

$$\mathbf{E}_p^{n+1} = \mathbf{E}_p^n + \left(\frac{2\varepsilon\Delta t + \sigma\Delta t^2}{2\varepsilon^2\Delta V}\right)\sum_{f\in\zeta_p}(\mathbf{n}\times\mathbf{H})_f^{n+1/2} + \frac{\sigma\Delta t^2}{\varepsilon^2\Delta V}\mathbf{G}_p^{n-1/2}, \tag{14}$$

$$\mathbf{G}_p^{n+1/2} = \mathbf{G}_p^{n-1/2} + \sum_{f\in\zeta_p}(\mathbf{n}\times\mathbf{H})_f^{n+1/2}\Delta S_f. \tag{15}$$

In this work, a second PML is introduced in the full field region of the waveguide to absorb the y-component of the magnetic field (H_y), the x-component of the electric field (E_x) and the z-component of the electric field (E_z). These fields must be absorbed before they reflect back into the scattered field region of the waveguide, otherwise the physics of the problem would not be satisfied. The implementation of the second PML in the full field is the same as the first PML, but the components that are absorbed are different. The second PML region has the same dimension as the first PML; however, it is located right at the end of the waveguide and near the cavity. This second PML allows the decoupling of the modes, and enables the propagation of only the TE_{10} mode, whilst all other modes that may exist in the full field region of the guide are absorbed.

Material interface conditions must be satisfied as the waves inside the free-space (D_1) propagate towards and reflect and refract at the material interface (D_2). The material boundary conditions are given as

$$\mathbf{n}\times(\mathbf{E}_{nb} - \mathbf{E}_p) = \mathbf{0}, \tag{16}$$

$$\mathbf{n}\cdot(\mathbf{D}_{nb} - \mathbf{D}_p) = 0, \tag{17}$$

$$\mathbf{n}\times(\mathbf{H}_{nb} - \mathbf{H}_p) = \rho, \tag{18}$$

$$\mathbf{n}\cdot(\mathbf{B}_{nb} - \mathbf{B}_p) = 0. \tag{19}$$

In Eqs. (16)–(19), $\mathbf{n}$ is the unit outward normal to the interface between free-space and the load. For most microwave heating problems the media are dielectric materials, which are current free. Hence, $\mu = \mu_0$ and $\rho = 0$, and Eqs. (16)–(19) give that the magnetic fields are continuous inside the whole problem domain (i.e., through the interface of D_1 and D_2), and the electric fields are discontinuous at material or load interfaces. The jump across the material interface is treated as in [20].

For both Maxwell's equations and the Helmholtz equation, perfectly conducting wall conditions have to be implemented. The only time this type of condition is not implemented in the Helmholtz equation is when the material does not touch the walls of the waveguide or the cavity. Hence, the treatment of the conducting wall boundary is crucial to both the time-domain and frequency domain solvers. At a perfectly conducting wall, the following criteria have to be satisfied:

$$\mathbf{E}\times\mathbf{n} = \mathbf{0}, \tag{20}$$

$$\mathbf{H}\cdot\mathbf{n} = 0. \tag{21}$$

According to (20) and (21), the tangential electric field and normal magnetic field components on a perfectly conducting wall are zero. The perfectly conducting wall conditions are implemented by creating spurious fields outside the free-space domain (D_1) for Maxwell's equation solver, and by catering for these in the discretisation for the Helmholtz equation solver [20].

2.4. Interior problem—Helmholtz equation

Inside the material depicted in Fig. 2 the Helmholtz equation is solved at a discrete frequency. The Helmholtz equation is developed and formulated from the time-harmonic electromagnetic equations as follows:

$$\nabla \times \xi = (\sigma + \mathrm{i}\omega\varepsilon)\phi, \tag{22}$$

$$\nabla \times \phi = -\mathrm{i}\omega\mu\xi. \tag{23}$$

In (22) and (23) $\xi \equiv H_i(f)$ and $\phi \equiv E_i(f)$, where $i = x, y, z$ denote the components of the magnetic and electric fields, respectively. By taking the curl of both equations and rearranging, the following Helmholtz equation is obtained for the electric fields:

$$\nabla^2\phi + \kappa^2\phi = 0, \tag{24}$$

$$\kappa^2 = \mu_0\omega(\omega\varepsilon - \sigma\mathrm{i}). \tag{25}$$

Eq. (24) satisfies the divergence criteria for constant material properties [7]:

$$\varepsilon\nabla \cdot \phi = 0. \tag{26}$$

It should be noted in this work that temperature dependent materials have not been used, and therefore, constant material properties have been assumed in the simulations. In the case when the material properties change with temperature, as heat is induced into the material by the presence of the electromagnetic waves, the divergence condition of Eq. (26) is no longer satisfied, and a new representation for Eq. (24) has to be obtained that takes into account permittivities that may change with changes in temperature.

The discretisation of the Helmholtz equation (22) is straightforward, and usually a second-order scheme is adapted to form the implicit system of linear equations. First, the Helmholtz equation from (24) is rewritten as

$$\nabla \cdot (\nabla\phi) + \kappa^2\phi = 0. \tag{27}$$

For a finite-volume discretisation strategy, (27) is integrated over the volume of the cell to give

$$\int_v \nabla \cdot (\nabla\phi)\partial v + \Delta V\kappa^2\bar{\phi} = 0, \tag{28}$$

where ΔV is the volume of the particular cell (Fig. 3). In (28), $\bar{\phi}$ is the average electric field for cell p:

$$\bar{\phi} = \frac{1}{\Delta V}\int_v \phi\,\partial V, \tag{29}$$

which is approximated as $\bar{\phi} \simeq \phi_p$. Hence, the discrete analogue of the volume integral (28) can be rewritten for cell p according to the following expression:

$$\sum_{f\in\zeta_p} (\nabla\phi \cdot \mathbf{n})_f \Delta S_f + \Delta V\kappa^2\phi_p = 0. \tag{30}$$

In (30) $\mathbf{n}$ is the unit outward normal on cell face f, ζ_p represents the set of faces that constitute cell p and the term $\nabla\phi \cdot \mathbf{n}$ is approximated on each of the faces of cell p. The mid-point integration rule was adopted for the integral approximation in (30), which is known to be second order accurate when the value of the unknown $(\nabla\phi \cdot \mathbf{n})_f$ is computed exactly. As a consequence of this limitation, an estimate of $\nabla\phi_f$ is sought on the cell face with high accuracy to enable the scheme to retain the second order spatial discretisation. On a Cartesian mesh, (29) is equivalent to the standard discretisation using

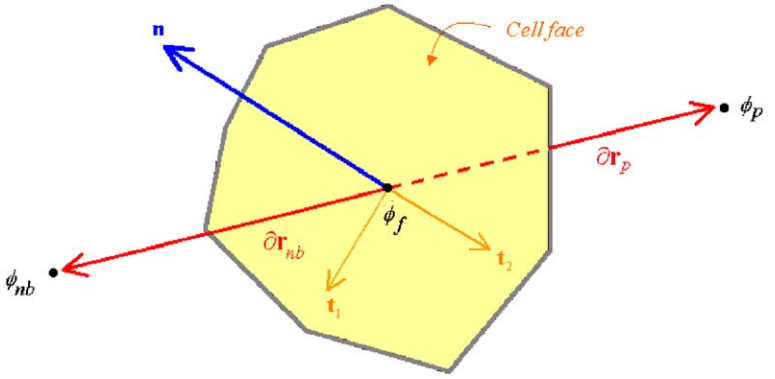

Fig. 3. A finite-volume cell face of a particular cell p.

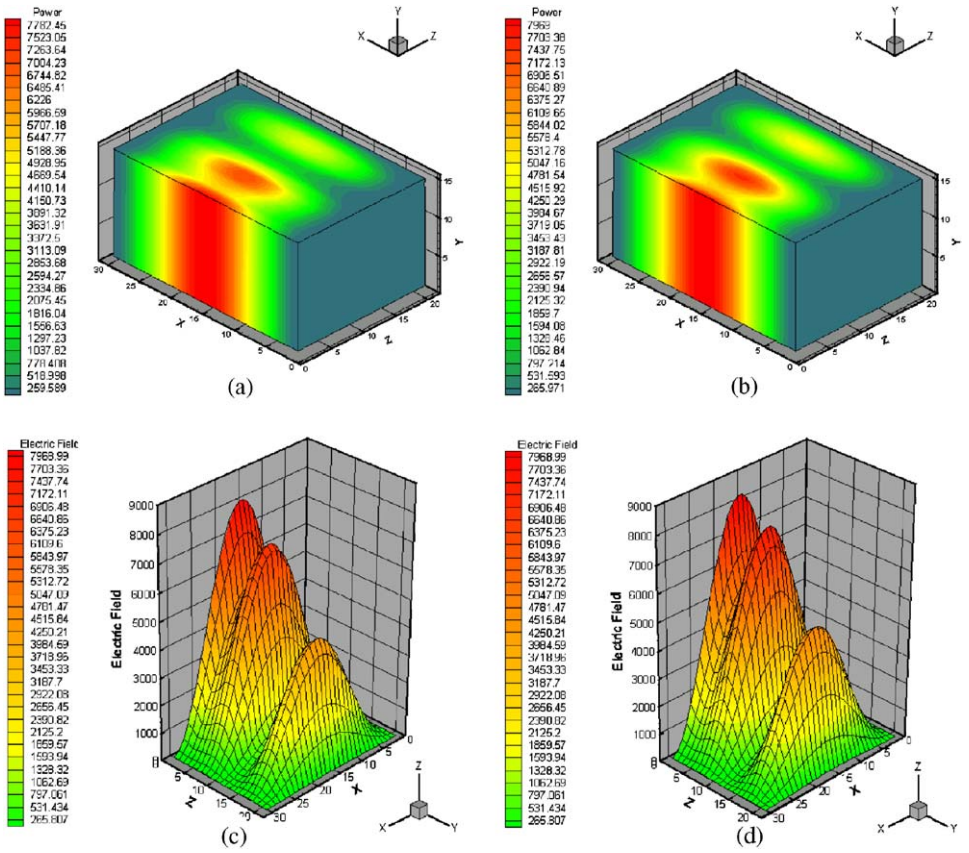

Fig. 4. Case study 1. Illustration of the loaded waveguide with load comprising 30 × 15 × 20 cells, (a) and (c) FD-TD power computation, (b) and (d) hybrid method power computation.

the Taylor approximations for $\nabla^2\phi$ in (24). Fig. 4 illustrates a particular face of the finite-volume cell for a component of the electric field ϕ. In the figure, $\mathbf{n}$ is the unit outward normal to face f, and $\mathbf{t}_1$ and $\mathbf{t}_2$ are unit vectors tangential to that face. The set of vectors $\{\mathbf{n}, \mathbf{t}_1, \mathbf{t}_2\}$ forms an orthonormal basis for $\mathbb{R}^3$. The vectors emanating from face f to ϕ_p and ϕ_{nb} are denoted by $\partial\mathbf{r}_p$ and $\partial\mathbf{r}_{nb}$, respectively. In (30), $\nabla\phi_f \cdot \mathbf{n}$ has to be approximated for a component of the electric field right on the cell face. To achieve this, the Taylor series is used to expand both ϕ_p and ϕ_{nb} about f, which

are written as

$$\phi_p = \phi_f + \partial\mathbf{r}_p \cdot \nabla\phi_f + \tfrac{1}{2}\partial\mathbf{r}_p^{\mathrm{T}} \mathscr{H}\, \partial\mathbf{r}_p + \cdots, \tag{31}$$

$$\phi_{nb} = \phi_f + \partial\mathbf{r}_{nb} \cdot \nabla\phi_f + \tfrac{1}{2}\partial\mathbf{r}_{nb}^{\mathrm{T}} \mathscr{H}\, \partial\mathbf{r}_{nb} + \cdots, \tag{32}$$

where $\mathscr{H}$ is the Hessian matrix for ϕ evaluated at the cell face. Subtracting (32) from (31) and letting $\partial\mathbf{r} = \partial\mathbf{r}_{nb} - \partial\mathbf{r}_p$, the following equation is obtained:

$$\phi_{nb} - \phi_p = \partial\mathbf{r} \cdot \nabla\phi_f + \tfrac{1}{2}[\partial\mathbf{r}_{nb}^{\mathrm{T}} \mathscr{H}\, \partial\mathbf{r}_{nb} - \partial\mathbf{r}_p^{\mathrm{T}} \mathscr{H}\, \partial\mathbf{r}_p] + \cdots. \tag{33}$$

Now, (33) can be rearranged to obtain the following equation:

$$\partial\mathbf{r} \cdot \nabla\phi_f \simeq (\phi_{nb} - \phi_p) - \varepsilon_f, \tag{34}$$

where

$$\varepsilon_f = \tfrac{1}{2}[\partial\mathbf{r}_{nb}^{\mathrm{T}} \mathscr{H}\, \partial\mathbf{r}_{nb} - \partial\mathbf{r}_p^{\mathrm{T}} \mathscr{H}\, \partial\mathbf{r}_p]. \tag{35}$$

To obtain $\nabla\phi \cdot \mathbf{n}$ at the face in (30), $\partial\mathbf{r}$ has to be resolved in terms of the orthonormal basis vectors in $\mathbb{R}^3$. Therefore, $\partial\mathbf{r}$ is represented as

$$\partial\mathbf{r} = (\partial\mathbf{r} \cdot \mathbf{n})\mathbf{n} + (\partial\mathbf{r} \cdot \mathbf{t}_1)\mathbf{t}_1 + (\partial\mathbf{r} \cdot \mathbf{t}_2)\mathbf{t}_2. \tag{36}$$

By operating on both sides of (36) with the dot product of $\nabla\phi_f$ and letting $\alpha_1 = \partial\mathbf{r} \cdot \mathbf{n}$, $\alpha_2 = \partial\mathbf{r} \cdot \mathbf{t}_1$ and $\alpha_3 = \partial\mathbf{r} \cdot \mathbf{t}_2$ the following expression is obtained:

$$\nabla\phi_f \cdot \partial\mathbf{r} = \alpha_1 \nabla\phi_f \cdot \mathbf{n} + \alpha_2 \nabla\phi_f \cdot \mathbf{t}_1 + \alpha_3 \nabla\phi_f \cdot \mathbf{t}_2. \tag{37}$$

Rearranging (37) for the $\nabla\phi_f \cdot \mathbf{n}$ term and substituting (34) gives the following expression:

$$\nabla\phi_f \cdot \mathbf{n} \simeq \frac{1}{\alpha_1}\left[\overbrace{(\phi_{nb} - \phi_p)}^{1}\ \underbrace{-\varepsilon_f - \alpha_2(\nabla\phi_f \cdot \mathbf{t}_1) - \alpha_3(\nabla\phi_f \cdot \mathbf{t}_2)}_{2}\right], \tag{38}$$

where it has been assumed that $\alpha_1 \neq 0$. In (38) term (1) is treated in an implicit manner while term (2) is treated explicitly. It should be noted, however, that the inclusion of term (2) in Eq. (38) for the gradient approximation introduces a non-linearity in (30) that requires special iterative treatment to obtain the solution for ϕ. In the case of Cartesian meshes, the inclusion of term (2) is not necessary. The approximation in (38) is used in (30) for the $(\nabla\phi \cdot \mathbf{n})_f$ term. To evaluate the right hand side in Eq. (38), a least squares approach can be adopted to approximate $\nabla\phi_f$ and the entries of the Hessian matrix for estimating the correction ε_f [5].

When all the cells in the computational domain have been visited with (30), the discretisation of the Helmholtz equation yields a system of linear equations for a component of the electric field ϕ at frequency k (ϕ^k), which is cast into matrix form as

$$\mathbf{A}\phi^k = \mathbf{b}. \tag{39}$$

In (39), $\mathbf{A}$ is the sparse coefficient matrix according to the discretisation of (24), and $\mathbf{b}$ is the right hand vector containing the boundary information generated using (6) with the time-domain data obtained from (4). Eq. (39) is solved three times for each frequency, because ϕ^k represents the three components of the electric field (i.e., $\phi^k \leftarrow \phi_x, \phi_y, \phi_z$). Once the electric field components in (39) have been obtained, the power is computed according to the following relationship:

$$P_p = \frac{\sigma_p}{2}\phi_p^2(f_k) = \frac{\sigma_p}{2}(\phi_x^2 + \phi_y^2 + \phi_z^2). \tag{40}$$

To obtain the power (P_p) at a particular node location p, (40) is computed after the electric field components have been obtained from (39). The solution to (39) is performed using Quasi-GMRES [15].

Algorithm 1 (*Quasi-GMRES*).

$r_0 = b - Ax_0, \quad \beta = \|r_0\|_2, \quad v_1 = r_0/\beta,$
for $j = 1$ *to* m
  $w = Av_j$
  for $i = max\{1, j - l + 1\}$ *to* j
    $h_{ij} = \langle w, v_i \rangle$
    $w = w - h_{ij} v_j$
  end for
  $h_{j+1,j} = \|w\|_2$
  if $h_{j+1,j} = 0$
    $m = j; \quad break$
  end if
  $v_{j+1} = w/h_{j+1,j}$
end for
$y_m = \min_y \|\beta e_1 - \bar{H}_m y\|_2$
$x_m = x_0 + V_m y_m$

Algorithm 1uses the modified Gram–Schmidt process for the orthogonalisation of the sub-space vectors within the i loop. In Quasi-GMRES, not all of the previously generated sub-space vectors were used in the reorthogonalisations, but rather, only a finite number (l) of them were used in the Gram–Schmidt process to obtain the next sub-space vector. As a consequence, as more and more sub-space vectors are computed, the amount of time taken to obtain the next best solution to the problem is bounded. For this problem it was found that a minimum of five reorthogonalisations ($l = 5$) of the generated sub-space vectors were required. The Quasi-GMRES method took considerably less time to compute than the standard GMRES solution strategy (where $l = m$). The computations here were investigated also using a set of 10 sub-space vectors for the reorthogonolisations, but no significant difference was observed, other than having to generate approximately 10% less vectors to reach the desired accuracy. The advantage of Quasi-GMRES over GMRES in this application is that the upper Hessenberg matrix ($\bar{H}_m$) becomes banded. As a consequence, the least-squares problem is solved also more rapidly. For the finer details of GMRES and Quasi-GMRES, the reader is referred to [14].

3. Results

In this section, a number of different case studies are analysed and the simulation results are compared to either the FD-TD scheme or experimentally determined thermal images. Firstly, a fully loaded waveguide is analysed where the material is placed so that it fills the waveguide. These results will be presented for a single mode waveguide, where the material or load cross-sectionally fills the short-circuit end of the guide. In such a case only the y-component of the electric field, and the x- and z-components of the magnetic field propagate.

Similarly to the first study, the second study concerns an inhomogeneously loaded waveguide, where the load half fills the cross-section of the waveguide and touches the x–z plane perfectly conducting wall. The modes inside the guide are studied, and the power distribution computed from the Helmholtz equation is compared to the highly accurate solution obtained via the FD-TD scheme. Fig. 1 exhibits the set-up for the different waveguide tests performed, whilst Fig. 12 illustrates the cavity and corresponding dimensions for case studies 3 and 4, where the hybrid method is validated against thermal images obtained from industrial applications.

For the waveguide problems, $a = 0.1$ m, $b = 0.05$ m and $c = 0.4$ m, while the PML region is $P = 0.09$ m deep and the input-plane is located at $z_0 = 0.1$ m. The location of the load will be given for the different case studies, along with the dielectric properties. In case studies 3 and 4, the dimensions for the waveguide, cavity and material are stated. The dielectric properties of the materials chosen in these case studies are indicative of lossy media, and hence, it is reasonable to assume that a large amount of the input energy is absorbed.

The power distribution is computed to compare the hybrid method with the FD-TD scheme. For the time and frequency domain comparisons, the power distribution is obtained in one of two ways. For the FD-TD solver, the power

at a point p is computed as a time-averaged value [23]:

$$P_p = \frac{1}{T}\int_{nT}^{(n+1)T} \sigma_p \mathbf{E}_p^2(t)\,\mathrm{d}t, \tag{41}$$

and for the hybrid method the power is computed according to (40). The difference between the two power computations lies in the representation of the electric field. All of the computations were performed on a dual processor PIII 1 GHz desktop computer with 512 MB of memory. Only one of the processors was used for the benchmark computations and the computational times quoted. The programs were written in the C/C++ programming language.

3.1. Case study 1—fully loaded waveguide

For the first case study, the average input power is set to $P_{\mathrm{av\_in}} = 500$ W and the permittivity of the load is $\varepsilon_r = 2 - \frac{1}{2}i$. The electric field amplitude that is used to excite the incident plane (8)–(10) is computed according to [3]

$$E_0 = \sqrt{\frac{2P_{\mathrm{av\_in}}\mu_0\omega}{\beta_0}}. \tag{42}$$

The material with dimension $0.1 \times 0.05 \times 0.1\ \mathrm{m}^3$ is placed inside the waveguide, touching the short-circuit end, so that the material cross-section fills the end of the full-field region of the guide. The standard boundary conditions are used as discussed in Section 2.3. The results have been computed for two different meshes; (a) the waveguide discretised into $30 \times 15 \times 80 = 36\,000$ cells with the load comprising $30 \times 15 \times 20 = 9000$ cells, and (b) the waveguide mesh consisting of $40 \times 20 \times 120 = 96\,000$ cells for which the load comprises $40 \times 20 \times 30 = 24\,000$ cells.

Figs. 4–7 exhibit the findings of the first study. Fig. 4 depicts the comparison of the power distribution when computed by the FD-TD scheme and the hybrid method for the coarser waveguide mesh (i.e., $30 \times 15 \times 20$), and Fig. 5 illustrates the results for the finer mesh ($40 \times 20 \times 30$). For both meshes, Figs. 6 and 7 illustrate the flood-contour plots and centre-line plots, respectively, for the two methods.

In this case study, the assumption of a TE_{10} mode was made, which implies that only the E_y, H_x and H_z components were present inside the waveguide. Therefore, the power computation using the hybrid method is somewhat simplified, as only the y-component of the electric field is computed.

For this case study the results were obtained after eight periods have elapsed in the time-marching of the electric and magnetic fields when the hybrid method was used. Once the boundary information for the interior problem was established, the power from the frequency domain electric field solution was obtained at the 2.45 GHz frequency. For the coarse mesh, the domain of the load was discretised into 9000 cells, while for the fine mesh the material was discretised into 24 000 cells. This meant that the matrix obtained from the Helmholtz equation stencil for both the coarse and fine meshes generated sparse matrices of dimension 9000×9000 and $24\,000 \times 24\,000$, respectively. The solution to the Helmholtz equation was very rapid, requiring the generation of 92 and 116 basis vectors for the coarse and fine meshes, respectively, for the GMRES solution. In the case of the FD-TD method to obtain a reasonably accurate solution, 14 periods were used to compute the electric and magnetic fields, out of which 2 periods were used to time-average the electric field for the power computations, whereas 8 periods were used for the hybrid method. As a consequence, the hybrid method for the waveguide problem is marginally quicker than the FD-TD scheme. Real gains are observed with the cavity problems, and these are outlined in the following three case studies. From Figs. 6 and 7 it can be seen that the main difference between the coarse and fine meshes is in the amplitude of the waves inside the material, and the phases of the waves are in agreement.

3.2. Case study 2—semi-loaded waveguide

This case study is very similar to the first problem; however, in this case the material has been cut into half, having dimension $0.05 \times 0.05 \times 0.1\ \mathrm{m}^3$. The material is placed against the short-circuit end of the waveguide and pushed to one side (see Fig. 1). The domain of the waveguide has been discretised using the same grid as before, where the coarse mesh consists of $15 \times 15 \times 20$ cells and the fine mesh consists of $20 \times 20 \times 30$ cells for the load.

As for the first case study in Section 3.1, Figs. 8 and 9 exhibit the power computations determined from the FD-TD and hybrid methods. The results are compared on both the coarse and fine meshes. In Fig. 10 the flood versus contour

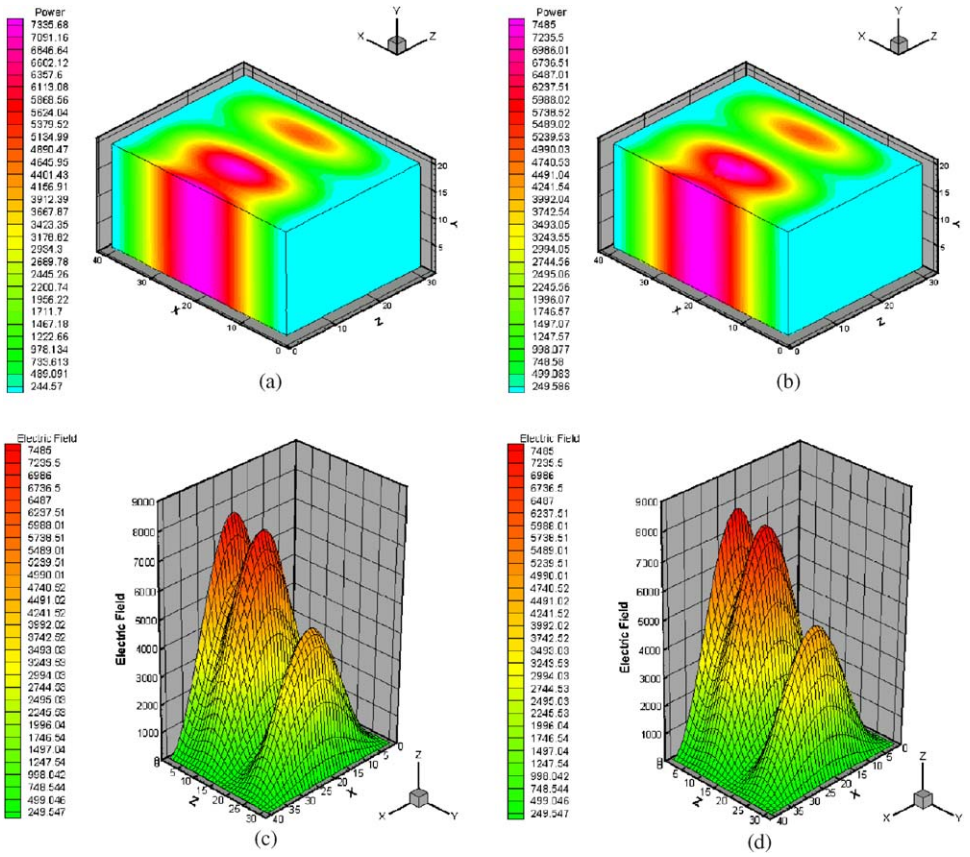

Fig. 5. Case study 1. Illustration of the loaded waveguide with load comprising $40 \times 20 \times 30$ cells, (a) and (c) FD-TD power computation, (b) and (d) hybrid method power computation.

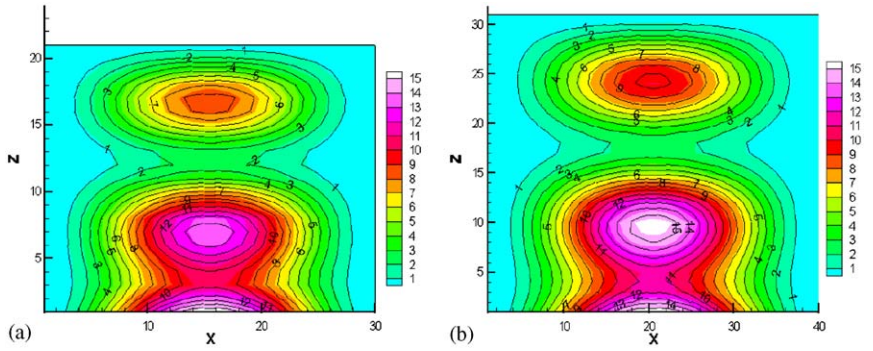

Fig. 6. Case study 1. Contour (FD-TD) versus flood (hybrid method) plots. (a) is load with $30 \times 15 \times 20$ cells and (b) is load with $40 \times 20 \times 30$ cells.

plots are given for the semi-loaded waveguide. The final illustration given in Fig. 11 is the centre-line plot of the power distribution computed using the hybrid method when compared to FD-TD. With the hybrid method the resultant numerical solutions tend to be smooth, due to the implicit nature of the solution strategy inside the material.

Unlike in the previous case study (see Section 3.1), here all field components $(H_x, H_y, H_z, E_x, E_y, E_z)$ have been computed and from the (E_x, E_y, E_z) field components the power distribution was obtained. It can be seen that when the waveguide is loaded at the short-circuit end, the results are in good agreement with the classical FD-TD methodology.

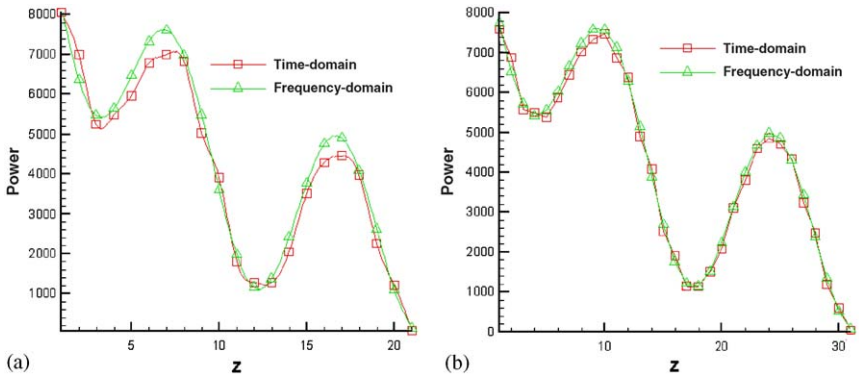

Fig. 7. Case study 1. Line plots of FD-TD (green) against hybrid method (red). (a) is load with $30 \times 15 \times 20$ cells and (b) is load with $40 \times 20 \times 30$ cells.

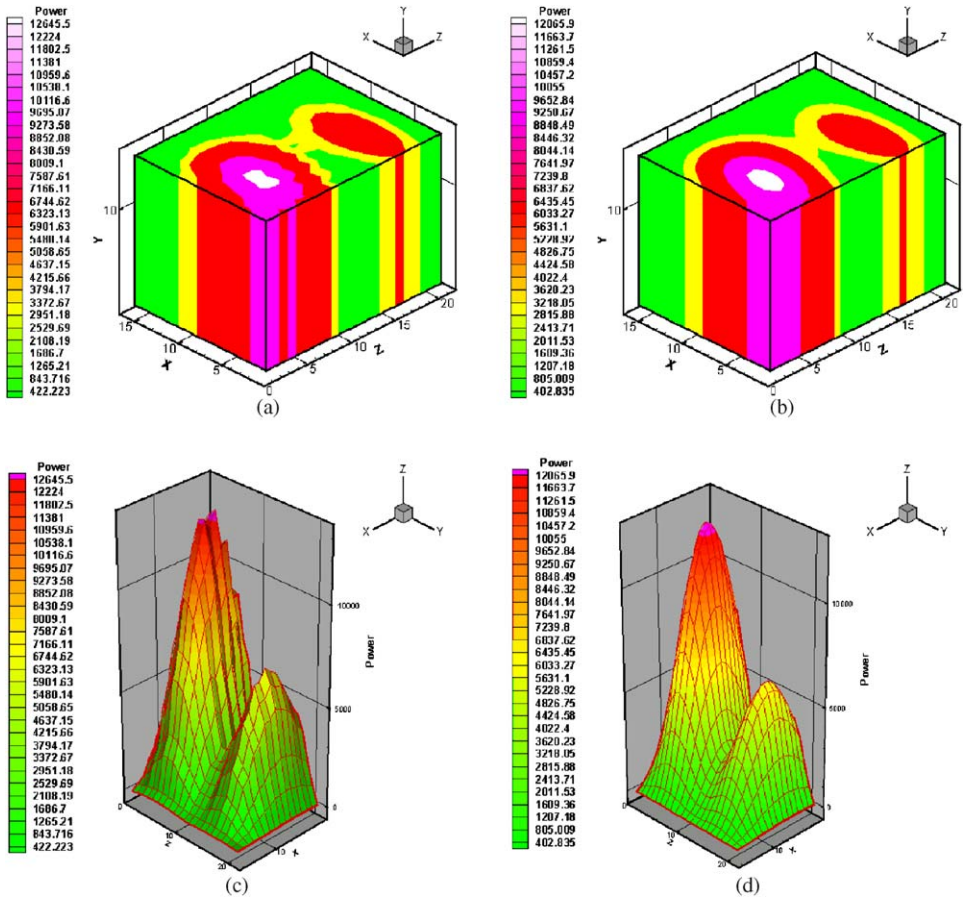

Fig. 8. Case study 2. Illustration of the loaded waveguide with load comprising $15 \times 15 \times 20$ cells, (a) and (c) FD-TD power computation, (b) and (d) hybrid method power computation.

In the waveguide case studies, the computational effort required to compute the power distribution using the hybrid method is similar to that of the FD-TD scheme. Here the grids were chosen to ensure that the FD-TD scheme was stable and provided reasonable solutions. The dimension of the coefficient matrix obtained using the Helmholtz equation

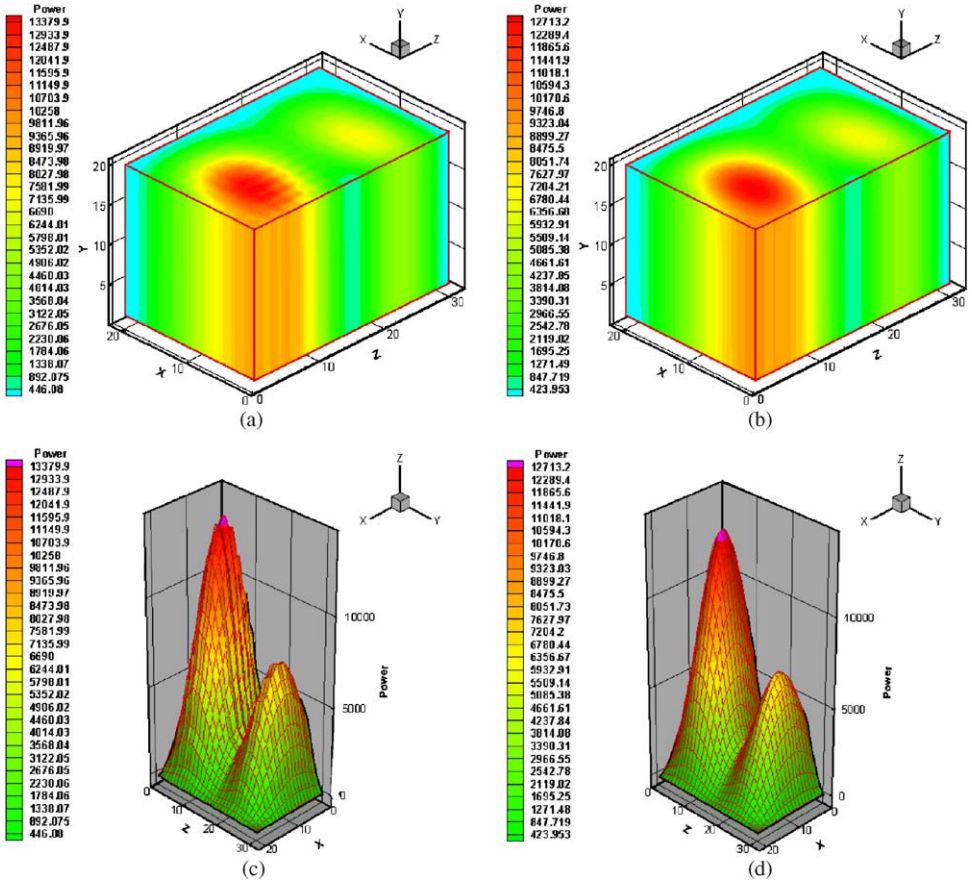

Fig. 9. Case study 2. Illustration of the loaded waveguide with load comprising 20 × 20 × 30 cells, (a) and (c) FD-TD power computation, (b) and (d) hybrid method power computation.

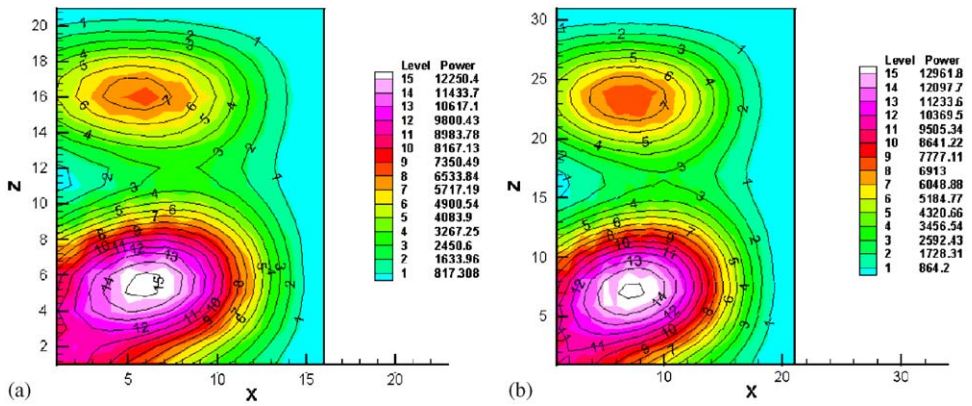

Fig. 10. Case study 2. Contour (FD-TD) versus flood (hybrid method) plots. (a) is load with 15 × 15 × 20 cells and (b) is load with 20 × 20 × 30 cells.

discretisation in the hybrid method was 4500 × 4500 for the coarse mesh and 12 000 × 12 000 for the fine mesh. In this case, 106 and 132 respective sub-space vectors were generated for the coarse and fine meshes to obtain the desired level of accuracy in the Helmholtz equation solution strategy. The same number of periods were run for both the FD-TD and

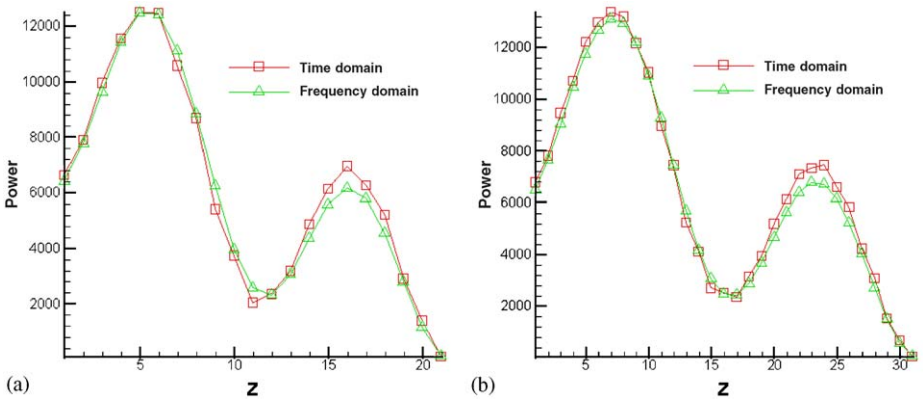

Fig. 11. Case study 2. Line plots of FD-TD (green) against hybrid method (red). (a) is load with $15 \times 15 \times 20$ cells and (b) is load with $20 \times 20 \times 30$ cells.

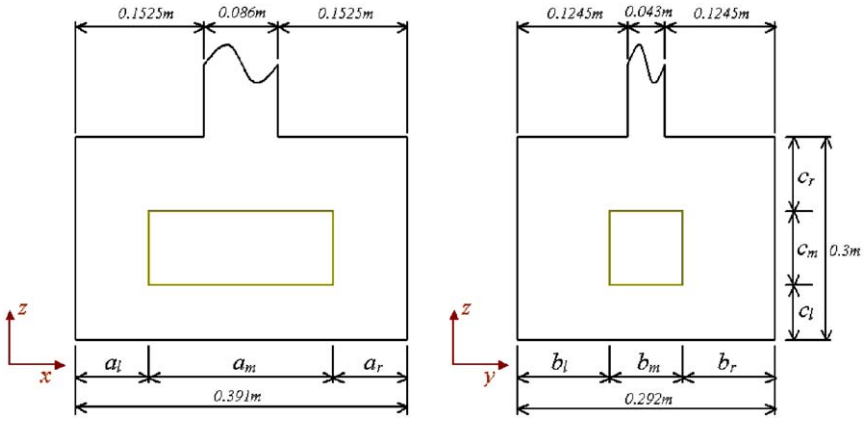

Fig. 12. The outline of the cavity problem.

hybrid methods as with case study 1. Moreover, the hybrid method produces results which are very accurate compared to the FD-TD method, and also, smooth due to the implicit nature of the scheme. The FD-TD simulations required 12 periods before the power distribution was obtained. The waveguide studies provide a benchmark for the hybrid method, and the following two case studies demonstrate the hybrid method using coarser grids on more realistic cavity microwave heating problems.

3.3. Case study 3—mashed potato

In this case study a cavity is attached to the short circuit end of the waveguide shown in Fig. 1. The waveguide has dimensions $0.086 \times 0.043 \times 0.16125\,\mathrm{m}^3$ and the cavity has dimensions $0.391 \times 0.292 \times 0.3\,\mathrm{m}^3$. The waveguide is attached to the top of the cavity as illustrated in Fig. 12. The centre-line of the waveguide lines up with the centre-line of the cavity. The mashed potato is located at the centre at the bottom of the cavity and has dimensions $0.21 \times 0.09 \times 0.03\,\mathrm{m}^3$. According to Fig. 12, the following parameters were used $a_l = a_r$, $a_m = 0.21\,\mathrm{m}$, $b_l = b_r$, $b_m = 0.09\,\mathrm{m}$, $c_l = 0\,\mathrm{m}$ and $c_m = 0.03\,\mathrm{m}$. It is assumed that the dielectric property of the mashed potato is constant throughout, and is given as $\varepsilon_r = 65 - 20i$. From the permittivity of this material it can be observed that it is lossy ($\varepsilon'' = 20$) and microwaves will have a high phase change at the material interface ($\varepsilon' = 65$).

The simulation results for this case study are graphically illustrated in Fig. 13. The thermal image [2] of the top surface of the mashed potato is given in Fig. 13(a). Fig. 13(b) illustrates the time-averaged electric field in the free-space

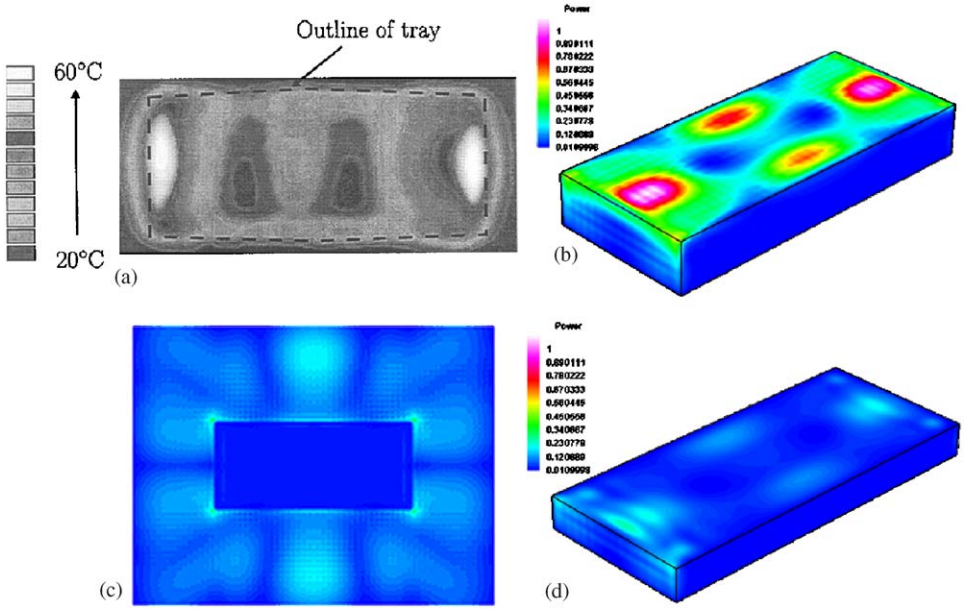

Fig. 13. Case study 3. Figure shows (a) thermal image of mashed potato [2], (b) time-averaged electric field distribution inside the cavity, (c) normalised power distribution obtained using the hybrid method at the surface and (d) normalised power distribution through the centre of the block as computed by the hybrid method.

component of the apparatus. Figs. 13(c) and (d) represent the results computed by the hybrid method at the surface and the middle of the block.

In this and the following case study, the power distribution inside the material has been illustrated, and compared directly to the thermal images. It should be noted that the power distribution is representative of the energy delivered to the material, and this energy will then manifest as dissipated heat. Heating will therefore occur in high energy areas. Due to the nature of the heating and the thermal material properties, the heat distribution is more dissipative and is expected to be less concentrated. The power distributions computed here are shown to capture the main aspects of the thermal images, which is thought to be a sufficient validation of the accuracy of the hybrid scheme.

It is evident from Fig. 13 that the hybrid method can adequately capture the nature of the power distribution when compared to the thermal image. Fig. 13(b) illustrates the computed time-averaged electric fields at the boundary of free-space and material. It can be seen from the figure that the heating occurs inside the material according to the time-averaged field computations.

In this case study the free-space component of the apparatus (including the material) was discretised into approximately 1 200 000 cells. The material itself contained around 59 000 cells. In the GMRES solution strategy 157 sub-space vectors were generated for the solution of each electric field component before a residual of less than 5×10^{-8} was obtained. As discussed earlier, Quasi-GMRES was used with 10 reorthogonalisations, which provided a sufficient gain in computational time (about 50%) as opposed to the standard GMRES method. The computations to obtain the approximate solution with the Quasi-GMRES method required approximately 20% more sub-space vector generations than with GMRES.

Approximately 148 min was required for the hybrid method to generate the boundary information for the interior problem. Once the boundary information had been obtained, the GMRES solution strategy calculated the power distribution in less than 5 min. Altogether, less than 160 min of computational time was required to obtain the power distribution. It should be noted that in the case of the hybrid method, only 16 electromagnetic wave periods were calculated in the exterior region using the time-domain solver. In the case of the FD-TD method, 50 electromagnetic wave periods have to be computed before reasonable power distribution estimates are obtained [22]. The FD-TD method also requires a finer mesh (i.e., at least 2 000 000 uniform cells), which would require approximately 480 min to compute. This time is extrapolated from timings documented in [20].

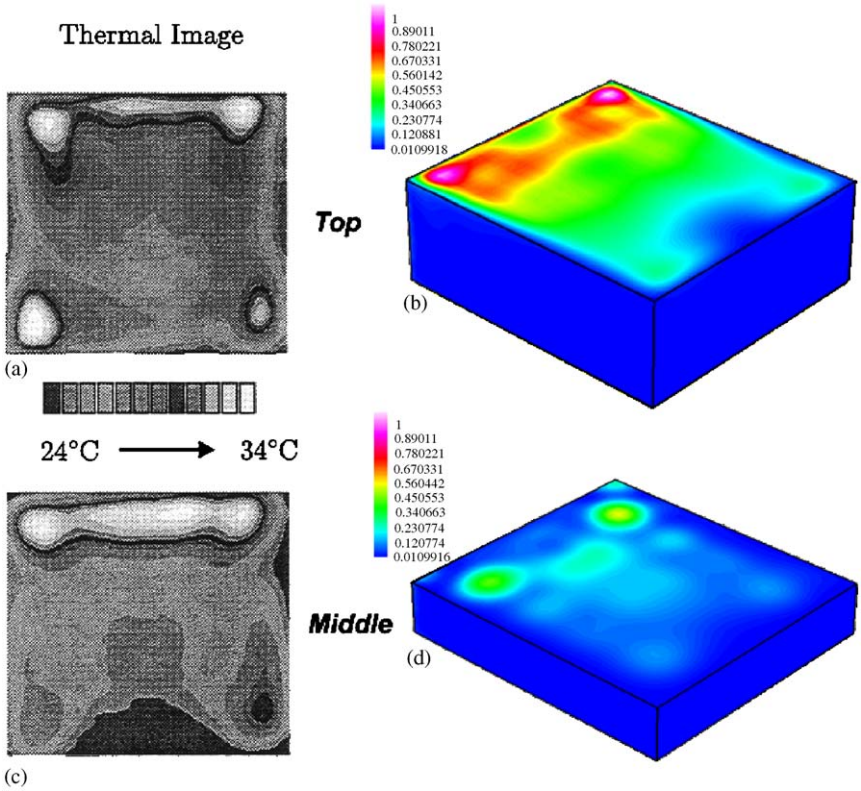

Fig. 14. Case study 4. Figure shows (a) thermal image of pastry layers at the surface [2], (b) normalised power distribution obtained using the hybrid method at the surface, (c) thermal image through the centre of the pastry [2] and (d) normalised power distribution through the centre as computed using the hybrid method.

3.4. Case study 4—layers of pastry

Considering the same cavity as for case study 3 (see Section 3.3) and the same waveguide, the power has been computed using the hybrid method for a pastry block. The pastry block consists of 11 layers of pastry, each 1 cm thick and laid closely on top of one another. The pastry block has a constant permittivity of $\varepsilon_r = 28 - 8i$. The dimensions of the pastry block are $0.11 \times 0.1 \times 0.04\,\mathrm{m}^3$. The block has been pushed to one side and raised 0.05 m from the bottom of the cavity. The pastry block is touching the $0.292 \times 0.3\,\mathrm{m}^2$ side of the cavity. According to Fig. 12, the following parameters were used for the simulations, $a_l = 0\,\mathrm{m}$, $a_m = 0.11\,\mathrm{m}$, $a_r = 0.281\,\mathrm{m}$, $b_l = b_r$, $b_m = 0.1\,\mathrm{m}$, $c_l = 0.05\,\mathrm{m}$ and $c_m = 0.04\,\mathrm{m}$ are the dimensions associated with this problem.

Fig. 14 illustrates the pastry block. In the figure, thermal images at two different cross sections are exhibited. The top and centre of the pastry block have been investigated, and the numerical solutions according to the hybrid method are shown next to the thermal images. In Fig. 14 it is evident that the hybrid method is capable of capturing the power generated in the block produced from the electromagnetic energy. In this work the hybrid method has been computed at a single frequency, which is a reasonable assumption for lossy materials [3].

In this case a mesh consisting of approximately 890 000 cells in the time-domain (including the material) was used to obtain the hybrid method numerical solution. The frequency-domain power distribution was obtained from 12 500 cells inside the load. To obtain reasonable and comparable solutions with the FD-TD method, at least 1 830 000 cells within the domain of the cavity are required [22]. Therefore, there is a large saving in time for the hybrid method.

For this case study involving the pastry block, the Helmholtz equation was solved implicitly using 12 500 unknown locations, which presented three systems of linear equations of dimension 12 500, for the E_x, E_y and E_z electric field components. Since the boundary information for the various electric field components for the linear systems was different, the number of sub-space reorthogonalisations varied in the GMRES method before convergence to a desired

level of accuracy (i.e., 5×10^{-8}) was achieved. Approximately 110 sub-space vectors were needed for each of the components to achieve the desired level of accuracy in the GMRES method. Quasi-GMRES was also investigated and took considerably less time to compute, but required around 130 sub-space vectors. The implementation of Quasi-GMRES saved a large amount of time, as it required around 220 s to compute the full GMRES, and took about 95 s to compute using the Quasi-GMRES method.

As in case study 3, only 16 electromagnetic wave periods were calculated in the exterior region of the problem before the power distribution was predicted using Quasi-GMRES (10 sub-space reorthogonalisations). Typically, it is necessary to run the FD-TD method in this cavity for around 50 electromagnetic wave periods before a reasonable power distribution is obtained [22].

From the studies conducted here the apparent limitation of the hybrid method remains in the time-domain solution strategy to generate sufficient boundary conditions for the solution of the frequency domain Helmholtz equation. Sufficiently large number of iterations are required in time to obtain a transient periodic behaviour to construct adequate frequency domain Dirichlet boundary conditions using the Fourier transform of time sequenced simulations. It should be noted that this remains an artifact of the solution strategy. Nevertheless, the hybrid method does provide the advantage of using less spatial grid points, as opposed to when the total domain of the problem is discretised, for example, using the FD-TD method.

4. Conclusions

In this paper a new hybrid method was presented for the microwave heating problem within a cavity. The hybrid method was outlined in detail and implemented on four different case studies. The first two case studies allowed the hybrid method to be benchmarked against the classical FD-TD scheme, whilst the final three case studies showed that the hybrid method produces realistic and reasonably accurate results for industrial type problems.

The power distribution obtained from the hybrid method was compared to two different thermal images, and was shown to be competitive with existing methods, and can produce results more quickly than the FD-TD scheme. The hybrid method has been formulated using an unstructured mesh terminology, but has been implemented here only on regular structured grids.

Future research will investigate the application of the proposed hybrid method when the properties of the material inside the microwave cavity change with temperature. Different grid structures for both the exterior and interior problems will also be investigated, which will require innovative interpolation techniques to capture the boundary information on the material interfaces. Higher order spatial approximations with the cell-centred SLF scheme will also be analysed with the hope of further reducing the number of grid points required to obtain the power distribution, so that even larger problems can be solved more readily.

Acknowledgements

The authors would like to acknowledge the use of the thermal images from Dr. David Dibben's thesis on finite element methods for the solution of microwave heating problems [2]. The thermal images for case studies 3 and 4 in Sections 3.3 and 3.4 were used in this work to compare the hybrid method to some specific problems. The authors would like to also thank Professor Yousef Saad for his input into fine tuning the GMRES method for this paper. With Professor Saad's help, large computational gains were realised in the solution of the Helmholtz equation.

References

[1] J.P. Berenger, Three-dimensional perfectly matched layer for the absorption of electromagnetic waves, J. Comput. Phys. 127 (1996) 363–379.
[2] D.C Dibben, Numerical and experimental modelling of microwave applicators, Ph.D. Thesis, Department of Engineering, University of Cambridge, 1995, p. 188.
[3] D.C. Dibben, A.C. Metaxas, Time domain finite element analysis of multimode microwave applicators loaded with low and high loss materials, International Conference on Microwave and High Energy Heating, vols. 1–3.4, 1995.
[4] S.D. Gedney, F. Lansing, Full wave analysis of printed microstrip devices using a generalized Yee-algorithm, IEEE Trans. 5 (1993) 1179–1182.
[5] P.A. Jayantha, I.W. Turner, A second order finite volume technique for simulating transport in anisotropic media, Internat. J. Numer. Methods for Heat and Fluid Flow 13 (1) (2003) 31–55.

[6] V.M. Kenkre, L. Skala, M.W. Weiser, J.D. Katz, Theory of microwave effects on atomic diffusion in sintering: basic considerations of the phenomenon of thermal runaway, in: W.B. Snyder, W.H. Sutton, M.F. Iskander, D.L. Johnson (Eds.), Microwave Processing of Materials, vol. II, Material Research Society Symposium Proceedings, vol. 189, Material Research Society, 1991, pp. 179–183.
[7] J.D. Kraus, D.A. Fleisch, Electromagnetics with Applications, McGraw-Hill, New York, 1999.
[8] G.A. Kriegsmann, Cavity effects in microwave heating of ceramics, SIAM J. Appl. Math. 57 (1997) 382–400.
[9] C.F. Lee, B.J. McCartin, R.T. Shin, J.A. Kong, A triangular-grid finite-difference time-domain method for electromagnetic scattering problems, J. Electromagnetic Waves and Applications 8 (4) (1994) 449–470.
[10] N.K. Madsen, R.W. Ziolkowski, A three-dimensional modified finite volume technique for Maxwell's equations, Electromagnetics 10 (1990) 147–161.
[11] A.C. Metaxas, R.J. Meredith, Industrial Microwave Heating, Peter Peregrinus Ltd., London, UK, 1983.
[12] P.G. Petropoulos, L. Zhao, A.C. Cangellaris, A reflectionless sponge layer absorbing boundary condition for the solution of Maxwell's equations with high-order staggered finite difference schemes, J. Comput. Phys. 139 (1998) 184–208.
[13] W.H. Press, S.A. Teukolsky, et al., Numerical Recipes in C: The Art of Scientific Computing, Cambridge University Press, Cambridge, 1997.
[14] Y. Saad, Iterative Methods for Sparse Linear Systems, <http://www-users.cs.umn.edu/~saad/>, 2000 (second edition with corrections).
[15] Y. Saad, Iterative Methods for Sparse Linear Systems, second ed., Society of Industrial and Applied Mathematics, Philadelphia, Penn., 2003.
[16] J.S. Shang, High-order compact-difference schemes for time-dependent Maxwell equations, J. Comput. Phys. 153 (1999) 312–333.
[17] V. Shankar, A.H. Mohammadian, A time-domain, finite-volume treatment for the Maxwell equations, J. Microwave Power and Electromagnetic Energy (1990) 128–145.
[18] V. Vegh, Numerical modelling of industrial microwave heating, Ph.D. Thesis, School of Mathematical Sciences, Queensland University of Technology, 2003.
[19] V. Vegh, I.W. Turner, A hybrid approach for resolving the microwave heating inside lossy media, Advances in Microwave and Radio Frequency Processing, Ampere 8, Germany, 2002.
[20] V. Vegh, I.W. Turner, H. Zhao, Effective cell-centred time-domain Maxwell's equations numerical solvers, Appl. Math. Modelling 29 (2005) 411–438.
[21] K.S. Yee, Numerical solution of initial boundary value problem involving Maxwell's equations in isotropic media, IEEE Trans. Antennas and Propagation 14 (1966) 302–307.
[22] H. Zhao, Computational Models and Numerical Techniques for Solving Maxwell's Equations: A Study of Heating of Lossy Dielectric Materials Inside Arbitrary Shaped Cavities, Centre in Statistical Science and Industrial Mathematics, Queensland University of Technology, Brisbane, 1997.
[23] H. Zhao, I.W. Turner, An analysis of the finite-difference time-domain method for modelling the microwave heating of dielectric materials within a three-dimensional cavity system, J. Microwave Power and Electromagnetic Energy 31 (4) (1996) 199–214.
[24] H. Zhao, I.W. Turner, The use of a coupled computational model for studying the microwave heating of wood, Appl. Math. Modelling 24 (3) (2000) 183–197.